J Therm Anal Calorim (2016) 125:423–435
DOI 10.1007/s10973-016-5450-6

Non-isothermal kinetics and mechanistic study of thermal decomposition of light rare earth metal nitrate hydrates using thermogravimetric analysis

Bamidele V. Ayodele[1,2,3] · Mohammed Anwar Hossain[1,3] · Soo Ling Chong[1] · Jiah Chee Soh[1] · Sureena Abdullah[1,3] · Maksudur R. Khan[1] · Chin Kui Cheng[1,2,3]

Received: 25 November 2015 / Accepted: 3 April 2016 / Published online: 11 April 2016

Abstract The formation of light rare earth metal oxides such as CeO_2, La_2O_3, Sm_2O_3, Nd_2O_3 and Pr_2O_3 from thermal decomposition of its nitrate precursors ($Ce(NO_3)_3{\cdot}6H_2O$, $La(NO_3)_3{\cdot}6H_2O$, $Sm(NO_3)_3{\cdot}6H_2O$, $Nd(NO_3)_3{\cdot}6H_2O$ and $Pr(NO_3)_3{\cdot}6H_2O$) have been investigated by thermogravimetric analysis. The rare earth metal oxides obtained were characterized for the nature of chemical bonds and textural properties using FTIR and N_2-physisorption analyses, respectively. The FTIR analysis of the rare earth metal precursors and the oxides showed that the OH– and NO– bonds depicting the presence of hydrated water molecules and nitrate disappeared after the thermal decomposition leaving out only the pure solid oxides. The kinetics data obtained from the thermogravimetric analysis were fitted into "model free" kinetic expressions such as Kissinger, Ozawa–Flynn–Wall to calculate the apparent activation energy of the solid-state decomposition reaction of the rare earth metal precursors. The kinetic parameters were further analyzed using Coat–Redfern model to determine the possible mechanism of the decomposition process. The calculated values of the activation energy obtained from both Kissinger and Ozawa–Flynn–Wall models were similar compared to that obtained from Coat–Redfern model. Highest activation energies of 230.26, 344.78, 320.2.78, 392.72 and 258.26 kJ mol^{-1} were obtained from decomposition of $Ce(NO_3)_3{\cdot}6H_2O$, $La(NO_3)_3{\cdot}6H_2O$, $Sm(NO_3)_3{\cdot}6H_2O$, $Nd(NO_3)_3{\cdot}6H_2O$ and $Pr(NO_3)_3{\cdot}6H_2O$), respectively, using Kissinger model, while the analysis of the kinetic data using Ozawa–Flynn–Wall model gave the highest activation energies of 229.01, 350.56, 348.56, 392.72 and 388.56 kJ mol^{-1} for decomposition of $Ce(NO_3)_3{\cdot}6H_2O$, $La(NO_3)_3{\cdot}6H_2O$, $Sm(NO_3)_3{\cdot}6H_2O$, $Nd(NO_3)_3{\cdot}6H_2O$ and $Pr(NO_3)_3{\cdot}6H_2O$), respectively. Thirteen different models were evaluated using Coat–Redfern models in order to determine the mechanisms that govern the decomposition process. Interestingly, two-dimensional diffusion mechanism with activation energy of 105.61, 107.61, 140.61, 144.52 and 154.78 kJ mol^{-1} was obtained for thermal decomposition of $Ce(NO_3)_3{\cdot}6H_2O$, $La(NO_3)_3{\cdot}6H_2O$, $Sm(NO_3)_3{\cdot}6H_2O$, $Nd(NO_3)_3{\cdot}6H_2O$ and $Pr(NO_3)_3{\cdot}6H_2O$), respectively. The rare earth metal oxides obtained from this study finds potential application as supports, promoters and catalysts in the field of catalysis.

Keywords Kinetics · Thermogravimetry analysis · Rare earth metals · Thermal decomposition · Solid-state reaction

✉ Chin Kui Cheng
chinkui@ump.edu.my

[1] Faculty of Chemical and Natural Resources Engineering, Universiti Malaysia Pahang, Lebuhraya Tun Razak, 26300 Gambang Kuantan, Pahang, Malaysia

[2] Rare Earth Research Centre, Universiti Malaysia Pahang, Lebuhraya Tun Razak, 26300 Gambang Kuantan, Pahang, Malaysia

[3] Centre of Excellence for Advanced Research in Fluid Flow, Universiti Malaysia Pahang, Lebuhraya Tun Razak, 26300 Gambang Kuantan, Pahang, Malaysia

Introduction

The interest in the use of rare earth metals for varieties of applications has increased tremendously since its discovery in 1787 by Karl Axel Arrhenius [1]. The rare earth metals are collection of 17 elements made of the lanthanoid group, viz. lanthanum (La), cerium (Ce), praseodymium (Pr), neodymium (Nd), promethium (Pm), samarium (Sm), europium (Eu), gadolinium (Gd), terbium (Tb), dysprosium (Dy), holmium (Ho), erbium (Er), thulium (Tm), ytterbium

(Yb), lutetium (Lu)), as well as scandium (Sc) and yttrium (Y) [2]. Reports by the US Geological survey in 2013 show that 65 % of rare earth metals are used in catalysis and the remaining 35 % are mainly used as alloy in metallurgy, for metal polishing and production of magnets.

Often, the lighter rare earth metals (Ce, La, Nd, Pr and Sm) come in nitrate compound form and may need to subject to thermal decomposition protocol before applications. The resulting oxides from the thermal decomposition of the rare earth metal nitrate hexahydrates find wide applications in catalysis as catalysts, promoters or supports. One major application of rare earth metal oxides as catalysts is for the purification of exhaust gases from vehicular emissions of poisonous pollutants such as carbon monoxides (CO), nitrogen oxides (NO_x) and particulate matters [3]. Moreover, rare earth metal oxides such as CeO_2, La_2O_3, Pr_2O_3, Nd_2O_3 and Sm_2O_3 have been reportedly used as catalyst for synthesis of unsaturated alcohol from dehydration of 1,4-butanediol and the synthesis of 2-propanol, propanone, methanol and ethanol from preferential decomposition of 1,3-butanediol [4–8]. Besides being used as catalysts, rare earth metal oxides have been extensively investigated as promoters in methane dry reforming [9, 10]. The findings from these studies showed that the use of rare earth metal oxides as promoters has significantly improved the stability of the catalysts toward carbon deposition. Nevertheless, one key area that is yet to be fully explored is the use of rare earth metal oxides as catalyst supports. In particular, one major advantage of using rare earth metal oxides as support is their oxygen storage capacity [3]. Although extensive study has been reported before on the use of rare earth metal oxides such as La_2O_3 and CeO_2 as support in reforming processes [11–18], rare earth metal oxides such as Nd_2O_3, Pr_2O_3 and Sm_2O_3 are yet to be investigated as support in heterogeneous catalytic reactions.

The synthesis of rare earth metal oxides from the decomposition of its nitrate hexahydrates precursors plays an important role in obtaining technological valuable materials. Studies on rare earth metal oxide formation from the thermal decomposition of rare earth metal precursors such as oxalates, oxychloride hydrates, chloride hydrates and nitrates were reported several decades ago [19–25]. These reported works focused mainly on the thermal decomposition of heavier rare earth metal precursors such as europium, terbium, dysprosium, holmium, erbium, thulium, ytterbium and lutetium chlorides hydrates. Furthermore, extensive review by Hessein [26] on the formation of rare earth metal oxides from thermal decomposition of acetate, oxalates and carboxylates of rare earth metals has been reported. All these studies only focused on the analysis of the features and stability of the intermediates as well as the gaseous products from the decomposition of the rare earth metal precursors.

In the present study, we report the mechanisms and kinetics of temperature-programmed decomposition of lighter rare earth metal nitrate hexahydrates, namely $Ce(NO_3)_3{\cdot}6H_2O$, $La(NO_3)_3{\cdot}6H_2O$, $Nd(NO_3)_3{\cdot}6H_2O$, $Sm(NO_3)_3{\cdot}6H_2O$ and $Ce(NO_3)_3{\cdot}6H_2O$. The mechanisms of the thermal decomposition of the rare earth metal nitrate hexahydrates were identified based on the thermogravimetric (TG) and differential thermogravimetric (DTG) results obtained from the thermogravimetric analysis. Kinetics parameters were estimated by fitting the non-isothermal TG data into solid-state reaction model-free expressions such as Kissinger [27] and Ozawa–Flynn–Wall [28] to determine the activation energy, and "model-fitting" expression such as Coats–Redfern for the mechanism of the solid-state decomposition reaction [29].

Experimental

The temperature-programmed decomposition of five lighter rare earth metal nitrate hexahydrates, namely $Ce(NO_3)_3{\cdot}6H_2O$, $La(NO_3)_3{\cdot}6H_2O$, $Nd(NO_3)_3{\cdot}6H_2O$, $Sm(NO_3)_3{\cdot}6H_2O$ and $Pr(NO_3)_3{\cdot}6H_2O$ (99.99 % trace metal basis, Sigma-Aldrich), were investigated using simultaneous thermogravimetric (TG, DTA) analyzer (STA 7000 Series). The measurements of the thermal decomposition of the rare earth metal nitrates hexahydrates under DTA-TG-DTG experimental conditions were carried out over a temperature ranged 298–1073 K at heating rates of 10, 15, 20 and 30 K min^{-1} in a flow of 50 mL min^{-1} of N_2. Furthermore, the rare earth metal oxides obtained from the thermogravimetric analysis, as well as the rare earth metal nitrate hexahydrates, were analyzed using Thermo Scientific FTIR spectrometer (Nicolet iS 50). Both samples were analyzed using attenuated total reflectance (ATR) method over wave number ranged 4000–400 cm^{-1} at a scanning rate of 0.02 cm^{-1}. The spectra were collected, processed and analyzed using Omnic series spectra analysis software. The textural properties of the rare earth metal oxides were measured using N_2 adsorption–desorption isotherm at 77 K using Thermo Scientific Surfer Analyzer according to standard BET procedure. The samples were degassed at 523 K for 3 h before the analysis. Barret–Joyner–Helenda (BJH) analysis method was employed to analyze the pore size distribution of the rare earth metal oxides from the N_2-desorption data.

Theoretical model

The rate of "conversion" of the rare earth metal nitrate hexahydrates $(d\alpha/dt)$ can be expressed as shown in Eq. (1) assuming $(d\alpha/dt)$ is proportional to the concentration of the precursors.

$$\frac{d\alpha}{dt} = kf(\alpha) \quad (1)$$

where k and $f(\alpha)$ are the rate constant and reaction model, respectively. The rate of "conversion" (α) of the rare earth metal nitrate hexahydrates and the rate constant are as in Eqs. (2) and (3), respectively.

$$\alpha = \frac{m_o - m_i}{m_o - m_f} \quad (2)$$

$$k = A\exp\left(\frac{-E}{RT}\right) \quad (3)$$

where m_o is the initial mass of the sample; m_f is the final mass of the sample; m_i is the mass of the sample at a given time; A is the pre-exponential factor; and R is the universal gas constant. The expression in Eq. (4) is obtained from the combination of Eqs. (1) and (3).

$$d\alpha/dt = A\exp\left(\frac{-E}{RT}\right)f(\alpha) \quad (4)$$

The thermal decomposition of the rare earth metal nitrate hexahydrates under a dynamic thermogravimetric analysis process (β is the heating ramping) gives the expression in Eq. (5).

$$d\alpha/dT = \frac{A}{\beta}\exp\left(\frac{-E}{RT}\right)f(\alpha) \quad (5)$$

Kinetic parameters of solid-state reaction can be estimated from the two fundamental Eqs. (4) and (5) using the non-isothermal TG data. In this study, the kinetic analysis of the temperature-programmed decomposition of the rare earth metal nitrate hexahydrates were investigated under dynamic conditions at heating rates of 10, 15, 20 and 30 K min^{-1}. The non-isothermal TG data obtained from the thermogravimetric analysis were fitted into "model-free" expressions such as Kissinger [27] and Ozawa–Flynn–Wall [28, 30] depicted in Eqs. (6) and (7). The mechanism of the solid-state decomposition reaction was further ascertained using Coats–Redfern [31] as in Eq. (8).

$$\ln\left(\frac{\beta}{T_p^2}\right) = \ln\left(\frac{AR}{E_a}\right) - \left(\frac{E_a}{RT_p}\right) \quad (6)$$

$$\ln\beta = \log\left(\frac{AE_a}{Rg(\alpha)}\right) - 2.315 - \frac{0.4567E_a}{RT} \quad (7)$$

$$\ln\left(\frac{g(\alpha)}{T_p^2}\right) = \ln\left(\frac{AR}{\beta E_a}\left(1 - \frac{2R\bar{T}}{E_a}\right)\right) - \left(\frac{E_a}{RT_p}\right) \quad (8)$$

The algebraic expressions listed in Table 1 are representations of the most common reaction mechanisms applicable in solid-phase decomposition reactions to be employed in Coats–Redfern expression.

Results and discussion

Temperature-programmed decomposition analyses

The TG-DTG and the DTA curves corresponding to the mass losses of the rare earth metal precursors under temperature-programmed condition and heating rates (β) of 10, 15, 20, 30 K min^{-1} are depicted in Fig. 1. The shapes of the TG–DTG curves are identical, irrespective of the heating rates. This signifies that the mass losses of the rare earth metal precursors do not vary with changes in heating rate [28, 32]. Generally, it can be seen from the DTG curves the occurrences of 3–4 stages of mass losses during the thermal decomposition process. These mass losses stages could be attributed to sequential loss in both physical and hydrated water, as well as decomposition of the nitrate species in the precursors ($Ce(NO_3)_3{\cdot}6H_2O$, $La(NO_3)_3{\cdot}6H_2O$, $Nd(NO_3)_3{\cdot}6H_2O$, $Sm(NO_3)_3{\cdot}6H_2O$ and $Pr(NO_3)_3{\cdot}6H_2O$) represented in Eqs. (9)–(13), respectively. The mass losses represented by the broad peaks (I) exhibiting maximum temperature at *circa* 400 K was characterized by an endothermic reaction as shown in the DTA curves (refers to Fig. 1). This signifies that there was a gain in thermal energy resulting in loss of physical water as well as the sequential dehydration of the hydrated water from the rare earth metal nitrate hexahydrates and the subsequent formation of anhydrous rare earth metal nitrate [33]. Furthermore, the mass losses corresponding to peaks II–IV (cf. Fig. 1) at temperatures ranged 550–900 K can be associated with an endothermic reaction (confirmed by the DTA curves), which corresponds to a successive thermal denitration of the anhydrous rare earth metal nitrate to form CeO_2, La_2O_3, Nd_2O_3, Sm_2O_3 and Pr_2O_3, respectively.

Non-isothermal decomposition of $Ce(NO_3)_3{\cdot}6H_2O$

$$Ce(NO_3)_3 \cdot 6H_2O \rightarrow Ce(NO_3)_3 + 6H_2O \quad \text{Peak I} \quad (9a)$$

$$Ce(NO_3)_3 \rightarrow Ce(NO_3)_2 + NO_2\uparrow + {}^1/_2O_2\uparrow \quad \text{Peak II} \quad (9b)$$

$$Ce(NO_3)_2 \rightarrow CeNO_3 + NO_2\uparrow + {}^1/_2O_2\uparrow \quad \text{Peak III} \quad (9c)$$

$$CeNO_3 \rightarrow CeO_2 + 2NO_2\uparrow \quad \text{Peak III} \quad (9d)$$

Non-isothermal decomposition of $La(NO_3)_3{\cdot}6H_2O$

$$La(NO_3)_3 \cdot 6H_2O \rightarrow La(NO_3)_3 + 6H_2O \quad \text{Peak I} \quad (10a)$$

$$La(NO_3)_3 \rightarrow La(NO_3)_2 + NO_2\uparrow + {}^1/_2O_2\uparrow \quad \text{Peak II} \quad (10b)$$

$$La(NO_3)_2 \rightarrow LaNO_3 + NO_2\uparrow + {}^1/_2O_2\uparrow \quad \text{Peak III} \quad (10c)$$

$$2LaNO_3 \rightarrow La_2O_3 + NO_2\uparrow + NO\uparrow \quad \text{Peak IV} \quad (10d)$$

Non-isothermal decomposition of $Nd(NO_3)_3{\cdot}6H_2O$

Table 1 Description of kinetic functions and mechanism used for the thermogravimetric analysis of the rare earth metal precursors

Model	$g(x)$	Rate controlling process
Power law (P2)	$x^{1/2}$	Chemical reaction
Power law (P3)	$x^{1/3}$	Chemical reaction
Power law (P4)	$x^{1/4}$	Chemical reaction
Avarami–Erofe'ev (A2)	$[-\ln(1-x)]^{1/2}$	Random nucleation and growth
Avarami–Erofe'ev (A3)	$[-\ln(1-x)]^{1/3}$	Random nucleation and growth
Avarami–Erofe'ev (A4)	$[-\ln(1-x)]^{3/4}$	Random nucleation and growth
Contracting area (R2)	$[1-(1-x)^{1/2}]$	Phase boundary reaction symmetry
Contracting area (R3)	$[1-(1-x)^{1/3}]$	Phase boundary reaction symmetry
One-dimensional diffusion (D1)	x^2	One-dimensional diffusion
Two-dimensional diffusion (D2)	$[(1-x)\ln(1-x)]+x$	Two-dimensional diffusion
Three-dimensional diffusion, Jander (D3)	$1-(1-x)^{\frac{1}{3}}]$	Three-dimensional diffusion
Ginstling–Brounshtein (D4)	$1-\left(\frac{2x}{3}\right)-(1-x)^{2/3}$	Three-dimensional diffusion spherical geometry
First order (F1)	$-\ln(1-x)$	Chemical reaction
Second order (F2)	$(1-x)^{-1}-1$	Chemical reaction
Third order (F3)	$[(1-x)^{-2}-1]/2$	Chemical reaction

$$Nd(NO_3)_3 \cdot 6H_2O \rightarrow Nd(NO_3)_3 + 6H_2O \quad \text{Peak I} \quad (11a)$$

$$Nd(NO_3)_3 \rightarrow Nd(NO_3)_2 + NO_2 \uparrow + {}^1\!/_2 O_2 \uparrow \quad \text{Peak II} \quad (11b)$$

$$Nd(NO_3)_2 \rightarrow NdNO_3 + NO_2 \uparrow + {}^1\!/_2 O_2 \uparrow \quad \text{Peak III} \quad (11c)$$

$$2NdNO_3 \rightarrow Nd_2O_3 + NO_2 \uparrow + NO \uparrow \quad \text{Peak IV} \quad (11d)$$

Non-isothermal decomposition of $Sm(NO_3)_3{\cdot}6H_2O$

$$Sm(NO_3)_3 \cdot 6H_2O \rightarrow Sm(NO_3)_3 + 6H_2O \quad \text{Peak I} \quad (12a)$$

$$Sm(NO_3)_3 \rightarrow Sm(NO_3)_2 + NO_2 \uparrow + {}^1\!/_2 O_2 \uparrow \quad \text{Peak II} \quad (12b)$$

$$Sm(NO_3)_2 \rightarrow SmNO_3 + NO_2 \uparrow + {}^1\!/_2 O_2 \uparrow \quad \text{Peak III} \quad (12c)$$

$$2Sm(NO_3) \rightarrow Sm_2O_3 + NO_2 \uparrow + NO \uparrow \quad \text{Peak IV} \quad (12d)$$

Non-isothermal decomposition of $Pr(NO_3)_3{\cdot}6H_2O$

$$Pr(NO_3)_3 \cdot 6H_2O \rightarrow Pr(NO_3)_3 + 6H_2O \quad \text{Peak I} \quad (13a)$$

$$Pr(NO_3)_3 \rightarrow Pr(NO_3)_2 + NO_2 \uparrow + {}^1\!/_2 O_2 \uparrow \quad \text{Peak II} \quad (13b)$$

$$Pr(NO_3)_2 \rightarrow Pr\,NO_3 + NO_2 \uparrow + {}^1\!/_2 O_2 \uparrow \quad \text{Peak III} \quad (13c)$$

$$2\,Pr(NO_3) \rightarrow \underset{2}{Pr}\,O_3 + NO_2 \uparrow + NO \uparrow \quad \text{Peak IV} \quad (13d)$$

FTIR and textural properties analyses of the rare earth oxides

The rare earth oxides obtained from the thermal decomposition of the respective metal precursors were subsequently analyzed using FTIR and N_2-physisorption. The FTIR spectra of the rare earth metal oxides (CeO_2, La_2O_3, Sm_2O_3, Nd_2O_3 and Pr_2O_3) in comparison with the respective precursors are depicted in Fig. 2. The FTIR spectra of the five rare earth metal precursors are identical in the nature of bonds formed, based on the bands of their respective peaks. Significantly, four types of bonds, namely O–H, N–O, C–O and M–O, can be identified from the FTIR spectra of the precursors as summarized in Table 2. The O–H stretching bond within wave number ranged 3386–3526 cm^{-1} can be attributed to the presence of hydrated and physical water. The N–O bond at wave number ranged 3185–3238 cm^{-1} can be attributed to the presence of nitrate species in the precursors. The C–O and M–O bonds at wave number ranged 1288–1644 and 629–652 cm^{-1}, respectively, can be attributed to the adsorbed atmospheric CO_2 and the rare earth metal–O stretching vibration. The spectra of the rare earth metal oxides obtained from the decomposition of the different precursors show disappearance of N–O and O–H bonds, signifying the removal of the hydrated water, as well as the decomposition of the nitrate species. The presence of the peaks at wave number 629–652 cm^{-1} corresponds to the

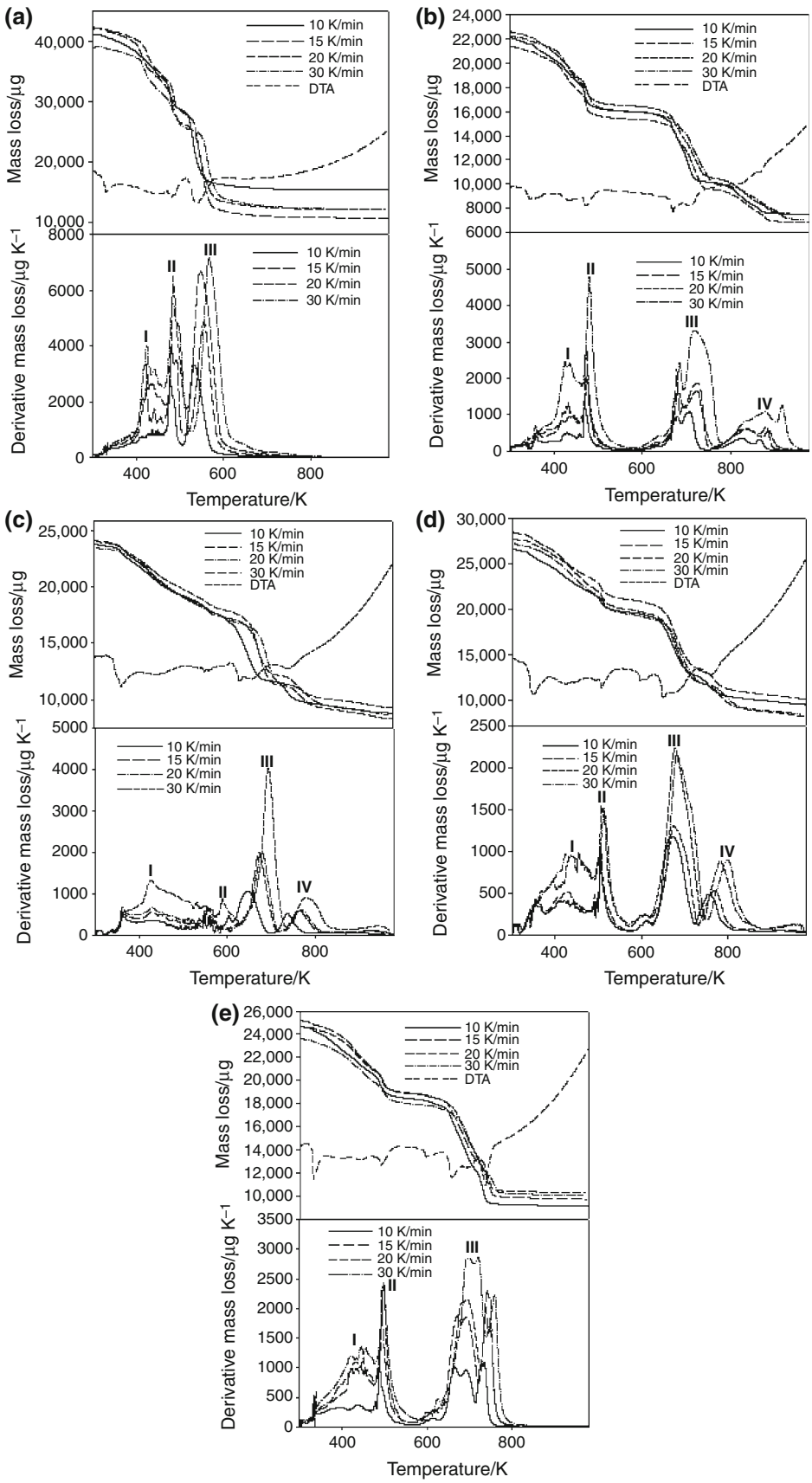

Fig. 1 TG-DTG and DTA plots for rare earth metal precursors: **a** $Ce(NO_3)_3{\cdot}6H_2O$, **b** $La(NO_3)_3{\cdot}6H_2O$, **c** $Sm(NO_3)_3{\cdot}6H_2O$, **d** $Nd(NO_3)_3{\cdot}6H_2O$, **e** $Pr(NO_3)_3{\cdot}6H_2O$

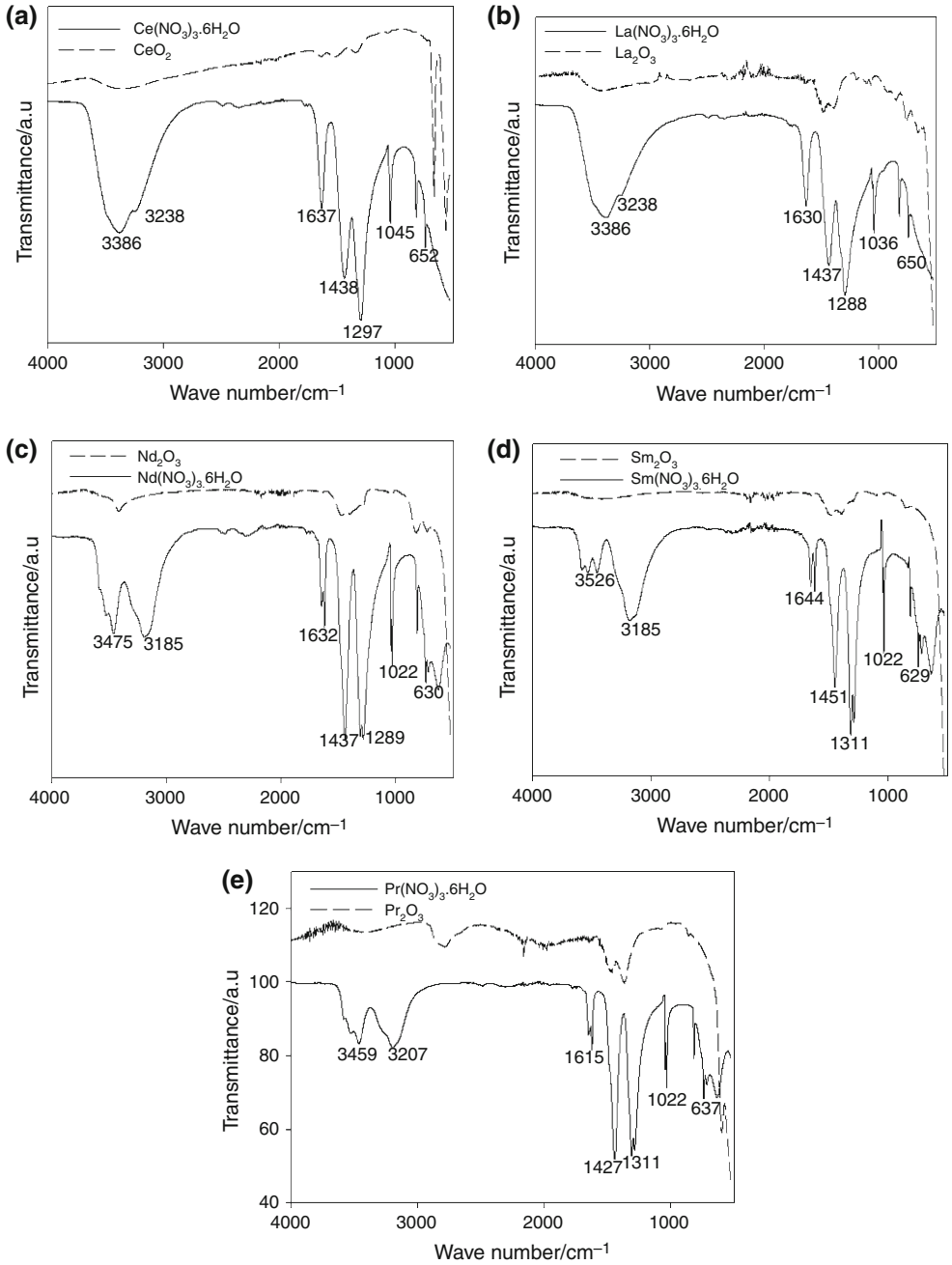

Fig. 2 Comparison between the FTIR spectra of the rare earth metal oxides and the precursors

formation of the respective rare earth metal oxides which can be affirmed by the disappearance of the DTG peaks at temperature >600, 900, 800, 800 and 750 K for decomposition of Ce-, La-, Sm-, Nd- and Pr-precursors, respectively [cf. Eqs. (9c), (10d), (11d), (12d) and (13d)]. The textural properties of the CeO_2, La_2O_3, Sm_2O_3, Nd_2O_3 and Pr_2O_3 formed from the thermal decomposition of the precursor were analyzed upon attainment of room temperature. The textural properties summarized in Table 3 shows that the BET-specific surface areas of 19.72, 8.33, 5.85, 9.19 and 12.03 $m^2\ g^{-1}$ were obtained for CeO_2, La_2O_3, Sm_2O_3, Nd_2O_3 and Pr_2O_3, respectively, with corresponding pore volumes of 0.0155, 0.0113, 0.0110, 0.0130 and 0.0311 $m^3\ g^{-1}$. The values of the specific surface area obtained for Nd_2O_3 and Pr_2O_3 are similar to 12.03 and 8 $m^2\ g^{-1}$ obtained by Hussein [34] and Balboul et al. [35] for the thermal decomposition of Neodymium acetate and Praseodymium acetate.

Table 2 FTIR analysis of the rare earth metal nitrate hexahydrates

Precursor	Base value	Bond	Comments
$Ce(NO_3)_3{\cdot}6H_2O$	3386	O–H	OH stretching vibration bond due to hydrated water
	3238	N–O	NO bond indicating the presence of nitrate
	1297–1637	C=O	CO bond due to dissolved atmospheric CO_2
	748–1045	M–O	MO bond represents the Ce–O stretching vibration
$La(NO_3)_3{\cdot}6H_2O$	3386	O–H	OH stretching vibration bond due to hydrated water
	3238	N–O	NO bond indicating the presence of nitrate
	1288–1630	C=O	CO bond due to dissolved atmospheric CO_2
	733–1036	M–O	MO bond represents the La–O stretching vibration
$Nd(NO_3)_3{\cdot}6H_2O$	3475	O–H	OH stretching vibration bond due to hydrated water
	3185	N–O	NO bond indicating the presence of nitrate
	1289–1632	C=O	CO bond due to dissolved atmospheric CO_2
	733–1022	M–O	MO bond represents the Nd-O stretching vibration
$Sm(NO_3)_3{\cdot}6H_2O$	3526	O–H	OH stretching vibration bond due to hydrated water
	3185	N–O	NO bond indicating the presence of nitrate
	1311–1644	C=O	CO bond due to dissolved atmospheric CO_2
	741–1022	M–O	MO bond represents the Sm–O stretching vibration
$Pr(NO_3)_3{\cdot}6H_2O$	3459	O–H	OH stretching vibration bond due to hydrated water
	3207	N–O	NO bond indicating the presence of nitrate
	1311–1615	C=O	CO bond due to dissolved atmospheric CO_2
	748–1022	M–O	MO bond represents the Pr–O stretching vibration

Thermal decomposition kinetics analysis of the rare earth metal precursors

Thermogravimetric data have been employed to evaluate kinetic parameters of solid-sate decomposition reactions as a function of mass loss [29]. The mass losses obtained from the thermal decomposition of the rare earth metal precursors as a function of four heating rates (10, 15, 20 and 30 °C min^{-1}) were further analyzed for evaluation of the kinetic parameters with the conversion of the rare earth metal precursors into its oxides counterparts. The data obtained from the thermogravimetric analysis were subjected to Kissinger, Ozawa–Flynn–Wall and Coats–Redfern solid-state kinetic models represented in Eqs. (6)–(8). The apparent activation energies of the non-isothermal decomposition of the rare earth metal precursors were obtained from the fittings of ln β/T^2 versus $1/T$ for Kissinger model, ln β versus $1/T$ for Ozawa's model and ln $g(x)/T^2$ versus $1/T$ for Coat–Redfern model, respectively. These fittings for each of the kinetic models are depicted in Fig. 3. The estimated activation energies, pre-exponential factors and coefficient of determinations obtained from the linear fittings of the three models are shown in Tables 4–9.

The Kissinger plots for the decomposition of $Ce(NO_3)_3{\cdot}6H_2O$, $La(NO_3)_3{\cdot}6H_2O$, $Sm(NO_3)_3{\cdot}6H_2O$ $Nd(NO_3)_3{\cdot}6H_2O$ and $Pr(NO_3)_3{\cdot}6H_2O$ are depicted in Fig. 3a–e respectively. The values of the activation energies obtained from the Kissinger's plots increase with removal of hydrated water. From Table 4, it can be seen that the activation energies obtained for the decomposition of $Ce(NO_3)_3{\cdot}6H_2O$ with peaks I, II and III are 104.61, 164.40 and 230.26 kJ mol^{-1}. Similar trends were exhibited by the decompositions of $La(NO_3)_3{\cdot}6H_2O$, $Nd(NO_3)_3{\cdot}6H_2O$, $Sm(NO_3)_3{\cdot}6H_2O$ and $Pr(NO_3)_3{\cdot}6H_2O$ with the corresponding activation energies

Table 3 Textural properties of the rare earth metal oxides

Textural properties	CeO_2	La_2O_3	Nd_2O_3	Sm_2O_3	Pr_2O_3
BET-specific surface area/m^2 g^{-1}	19.72	8.33	5.87	9.19	12.03
Cumulative pore area/m^2 g^{-1}	11.24	7.34	7.55	9.14	14.04
Cumulative pore volume/m^3 g^{-1}	0.0155	0.0113	0.0110	0.0130	0.0322
Average pore diameter/nm	1.47	1.14	1.25	1.41	1.53

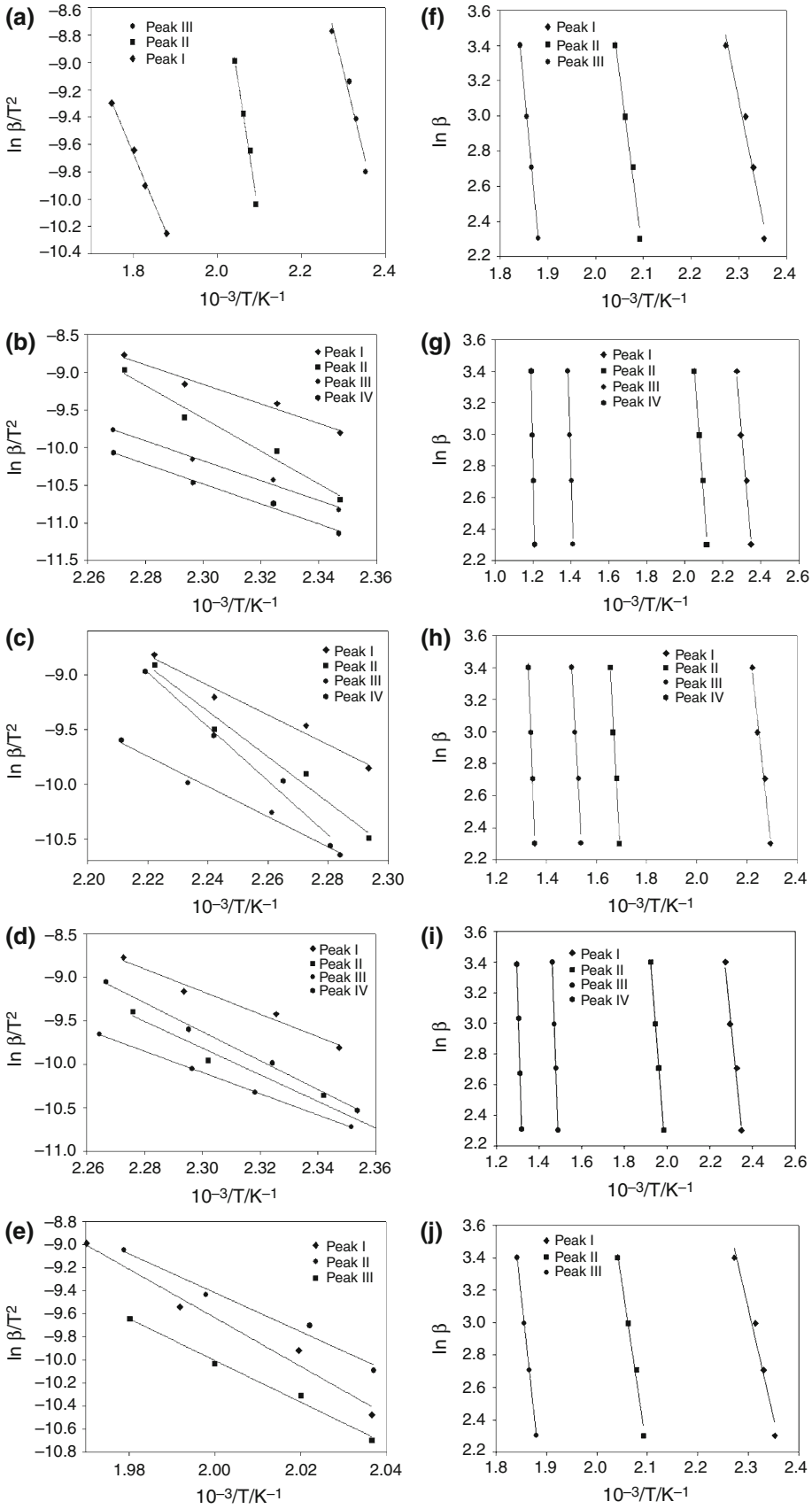

Fig. 3 Estimation of activation energies using Kissinger for **a** $Ce(NO_3)_3{\cdot}6H_2O$, **b** $La(NO_3)_3{\cdot}6H_2O$, **c** $Sm(NO_3)_3{\cdot}6H_2O$, **d** $Nd(NO_3)_3{\cdot}6H_2O$ and **e** $Pr(NO_3)_3{\cdot}6H_2O$ and Ozawa–Flynn–Wall for **f** $Ce(NO_3)_3{\cdot}6H_2O$, **g** $La(NO_3)_3{\cdot}6H_2O$, **h** $Sm(NO_3)_3{\cdot}6H_2O$, **i** $Nd(NO_3)_3{\cdot}6H_2O$ and **j** $Pr(NO_3)_3{\cdot}6H_2O$

Table 4 Kinetics parameters of the temperature-programmed calcination of $Ce(NO_3)_3{\cdot}6H_2O$

Parameters	I	II	III
Kissinger kinetics model			
E_a/kJ mol^{-1}	104.61	164.40	230.26
A	4.31×10^8	4.33×10^{13}	2.9×10^{29}
R^2	0.96	0.98	0.99
SEE	0.092	0.047	0.047
Ozawa–Flynn–Wall kinetics model			
E_a/kJ mol^{-1}	106.16	161.14	229.01
A	3.48×10^9	1.05×10^{14}	9.83×10^{28}
R^2	0.97	0.99	0.99
SEE	0.092	0.047	0.047

SEE standard error of estimate

for each peak summarized in Tables 5–8, respectively. Peak I which signifies the loss of water has the lowest activation energies for the decomposition of all the rare earth metal precursors. The nitrate decomposition represented by peaks III for decomposition of $Ce(NO_3)_3{\cdot}6H_2O$ and $Pr(NO_3)_3{\cdot}6H_2O$ as well as peak IV represented by decomposition of $La(NO_3)_3{\cdot}6H_2O$, $Nd(NO_3)_3{\cdot}6H_2O$ and $Sm(NO_3)_3{\cdot}6H_2O$, respectively, recorded higher values of activation energies (230.26, 344.78, 320.52, 392.72 and 258.26 kJ mol^{-1}, respectively). The value of activation energy obtained for the decomposition of $Ce(NO_3)_3{\cdot}6H_2O$ is higher compared to that 104 kJ mol^{-1} obtained by Strydom and Vuuren [33] from thermal decomposition of anhydrous $Ce(NO_3)_3$. The higher value of apparent activation energy in this study could be as a result of the presence of hydrated water in the precursor as well as difference in decomposition atmosphere; N_2 was used in this study contrary to Ar reported by the authors. Furthermore, the values of activation energies obtained from the decomposition of the various rare earth metal precursors using Ozawa–Flynn–Wall kinetic model are also summarized in Tables 4–8. The activation energies obtained using both Kissinger's and Ozawa–Flynn–Wall kinetic models are almost similar. Moreover, the activation energies obtained from the kinetic data using Ozawa–Flynn–Wall model increased with the removal of the hydrated waters. This implies that higher thermal energy is required as the hydrated water molecule is reduced [36]. Comparing the kinetics parameters obtained from this study with the literature, the activation energy of the solid-state decomposition is dependent on the nature of the rare earth metal precursors as well as chemical bonds. Aril et al. [37] obtained activation energy of 140 kJ mol^{-1} for the thermal decomposition of Cerium (III) acetate hydrate ($Ce(CH_3CO_2)_3{\cdot}1.5H_2O$ using thermogravimetric analysis. The authors reported four decomposition steps of the ($Ce(CH_3CO_2)_3{\cdot}1.5H_2O$ to CeO_2 at temperature ranged 573–997 K. Similarly, Premkumar et al. [38] investigated the thermal decomposition of hydrazinium cerium 2,3-Pyrazinedicarboxylate hydrate to CeO_2. The authors reported activation energy of *circa* 160 kJ mol^{-1} from the kinetic data. Todorovsky et al. [39] reported that the thermal decomposition of La-precursor (La-Ti-non-crystalline citric complexes) to $La_2Ti_2O_7$ using thermogravimetric analysis. Four stages were observed during the thermal decomposition process which is in good agreement with the thermal decomposition of $La(NO_3)_3{\cdot}6H_2O$ reported in this study.

Mechanism of the solid-state decomposition

The solid-state kinetic data of the decomposition of the rare earth metal precursors obtained from the thermogravimetric analysis were further evaluated using the Coat–Redfern models. Apparent activation energies for the decomposition reaction of the various rare earth metal precursors were estimated from the Coat–Redfern method using 13 models

Table 5 Kinetics parameters of the temperature-programmed calcination of $La(NO_3)_3{\cdot}6H_2O$

Parameters	I	II	III	IV
Kissinger kinetics model				
E_a/kJ mol^{-1}	107.71	128.62	225.29	344.78
A	9.14×10^8	7.47×10^9	3.19×10^{13}	4.50×10^{19}
R^2	0.98	0.99	0.98	0.99
SEE	0.092	0.047	0.047	0.047
Ozawa–Flynn–Wall kinetics model				
E_a/kJ mol^{-1}	108.16	129.14	229.01	350.56
A	3.48×10^9	1.05×10^8	9.83×10^{12}	8.18×10^{20}
R^2	0.96	0.99	0.99	0.99
SEE	0.092	0.047	0.047	0.046

SEE standard error of estimate

Table 6 Kinetics parameters of the temperature-programmed calcination of $Nd(NO_3)_3{\cdot}6H_2O$

Parameters	I	II	III	IV
Kissinger kinetics model				
E_a/kJ mol^{-1}	112.91	225.29	230.65	320.20
A	1.83×10^{9}	3.18×10^{15}	7.11×10^{15}	4.50×10^{19}
R^2	0.98	0.99	0.98	0.99
SEE	0.092	0.047	0.047	0.047
Ozawa–Flynn–Wall kinetics model				
E_a/kJ mol^{-1}	113.16	226.14	229.01	348.56
A	3.48×10^{10}	1.05×10^{16}	9.83×10^{16}	8.18×10^{20}
R^2	0.96	0.99	0.99	0.99
SEE	0.092	0.047	0.047	0.046

SEE standard error of estimate

Table 7 Kinetics parameters of the temperature-programmed calcination of $Sm(NO_3)_3{\cdot}6H_2O$

Parameters	I	II	III	IV
Kissinger kinetics model				
E_a/kJ mol^{-1}	107.71	141.50	331.08	392.72
A	9.14×10^{9}	1.81×10^{11}	1.21×10^{21}	1.90×10^{22}
R^2	0.98	0.99	0.99	0.99
SEE	0.092	0.047	0.047	0.047
Ozawa–Flynn–Wall kinetics model				
E_a/kJ mol^{-1}	108.16	151.14	329.01	388.56
A	3.48×10^{10}	1.05×10^{12}	9.83×10^{23}	8.18×10^{24}
R^2	0.96	0.99	0.99	0.99
SEE	0.092	0.047	0.047	0.046

SEE standard error of estimate

Table 8 Kinetics parameters of the temperature-programmed calcination of $Pr(NO_3)_3{\cdot}6H_2O$

Parameters	I	II	III
Kissinger kinetics model			
E_a/kJ mol^{-1}	122.49	148.32	258.26
A	1.11×10^{11}	2.58×10^{38}	4.42×10^{15}
R^2	0.96	0.99	0.99
SEE	0.092	0.047	0.047
Ozawa–Flynn–Wall kinetics model			
E_a/kJ mol^{-1}	123.16	151.14	259.01
A	3.48×10^{12}	1.05×10^{39}	9.83×10^{17}
R^2	0.96	0.99	0.99
SEE	0.092	0.047	0.047

SEE standard error of estimate

in order to determine a suitable mechanism that best describe the solid-state reaction. The kinetic data of the decomposition reaction were analyzed from Coat–Redfern model with the mechanisms being controlled by chemical reaction governed by power law (P2–P3), random nucleation and growth (A2–A4), phase boundary reaction (R2–R3), dimensional dimension (D1–D4) and chemical reaction based on the order of reaction (F1–F3). The activation

Table 9 Activation energy of the solid-state kinetics of the rare earth precursors obtained from Coats–Redfern expression using different mechanisms

Model	$Ce(NO_3)_3{\cdot}6H_2O$			$La(NO_3)_3{\cdot}6H_2O$			$Nd(NO_3)_3{\cdot}6H_2O$			$Sm(NO_3)_3{\cdot}6H_2O$			$Pr(NO_3)_3{\cdot}6H_2O$		
	E_a^a	R^2	A/S^{-1}	E_a^a	R^2	A/S^{-1}	E_a^a	R^2	A/S^{-1}	E_a^a	R^2	A/S^{-1}	E_a^a	R^2	A/S^{-1}
P2	104.61	0.96	6.21×10^9	106.61	0.95	8.22×10^{12}	111.22	0.96	9.32×10^{15}	124.32	0.94	8.12×10^{11}	113.33	0.95	7.33×10^{13}.
P3	105.02	0.94	5.41×10^8	101.02	0.93	9.41×10^{10}	105.38	0.97	8.31×10^{10}	105.78	0.96	9.42×10^{12}	118.78	0.95	11.42×10^{14}
P4	104.02	0.96	7.2×10^8	103.02	0.96	7.32×10^8	115.02	0.95	6.32×10^{10}	125.51	0.95	7.21×10^{12}	125.42	0.96	$5.43 \times . 10^{14}$
A2	87.02	0.97	6.31×10^8	90.02	0.98	7.67×10^9	105.02	0.96	8.67×10^{12}	115.34	0.93	8.88×10^{13}	105.76	0.94	7.32×10^{11}
A3	98.9	0.95	7.43×10^9	95.5	0.94	9.71×10^9	113.90	0.97	10.71×10^{13}	133.92	0.95	6.81×10^{11}	113.34	0.93	5.32×10^{14}
A4	87.98	0.93	5.31×10^8	85.78	0.96	5.31×10^{11}	103.18	0.93	7.21×10^{11}	113.98	0.96	7.87×10^{12}	131.74	0.94	9.37×10^{11}
R2	83.41	0.84	6.37×10^9	80.31	0.88	6.97×10^8	123.41	0.89	6.43×10^8	123.51	0.90	8.88×10^{13}	133.41	0.90	8.72×10^{12}
R3	66.77	0.91	8.72×10^8	72.47	0.92	8.81×10^7	120.78	0.95	7.21×10^9	120.51	0.92	9.53×10^{12}	120.54	0.93	7.13×10^{16}
D1	83.82	0.90	9.38×10^7	81.12	0.94	8.36×10^8	103.87	0.96	7.86×10^8	103.82	0.95	8.53×10^{11}	125.42	0.97	9.65×10^{13}
D2	105.61	0.99	7.26×10^9	107.61	0.99	8.88×10^9	140.61	0.98	9.42×10^{16}	144.52	0.99	10.12×10^{14}	158.51	0.98	11.15×10^{16}
D3	80.61	0.91	8.44×10^8	83.62	0.93	6.65×10^9	109.64	0.96	7.75×10^8	124.74	0.95	8.43×10^9	130.42	0.94	9.13×10^{10}
D4	100.61	0.96	6.51×10^8	103.41	0.97	7.89×10^{10}	124.71	0.96	9.79×10^{10}	132.52	0.96	6.78×10^{13}	127.42	0.95	7.18×10^{11}
F1	91.02	0.95	9.52×10^8	94.42	0.95	9.87×10	135.52	0.96	6.89×10^{12}	125.02	0.95	8.83×10^{14}	119.21	0.97	9.63×10^{13}
F2	65.2	0.94	5.11×10^8	69.02	0.95	10.11×10^8	135.28	0.96	11.21×10^{10}	136.20	0.96	10.31×10^{11}	135.56	0.96	8.23×10^{12}
F3	85.2	0.92	6.21×10^8	88.31	0.93	8.90×10^8	115.26	0.96	9.90×10^{11}	125.32	0.96	8.70×10^{12}	127.76	0.96	9.30×10^{14}

[a] The unit of activation energy E_a is kJ mol^{-1}

energies, the pre-exponential factors and the coefficient of determination are summarized in Table 9. Highest activation energies of 105.61, 107.61, 140.61, 144.52 and 154.78 kJ mol^{-1} were calculated for the thermal decomposition of $Ce(NO_3)_3{\cdot}6H_2O$, $La(NO_3)_3{\cdot}6H_2O$, $Nd(NO_3)_3{\cdot}6H_2O$, $Sm(NO_3)_3{\cdot}6H_2O$ and $Pr(NO_3)_3{\cdot}6H_2O$, respectively, using two-dimensional diffusion mechanism. The values of the R^2 (close to unity) obtained for the dimensional diffusion mechanism (model D2) depicted in Table 9 imply that the thermal decomposition reaction of the rare earth metal precursors can best describe the mechanism. Based on the dimensional diffusion mechanism, it is most likely that the gaseous components of the thermal decomposition reaction required higher temperature to be released and hence more energy which further substantiates the higher activation energy obtained for the decompositions of each of the rare earth metal precursors.

The mechanism obtained for the thermal decomposition of $Sm(NO_3)_3{\cdot}6H_2O$ in this study is corroborated by that reported by Hussein et al. [40]. Four stages which include loss of physical water as well as sequential loss of hydrated water and the decomposition of the $Sm(NO_3)_3$ to Sm_2O_3 and nitrous oxides were reported by the authors. Furthermore, the sequence of decomposition of $Nd(NO_3)_3{\cdot}6H_2O$ reported by Kepinski et al. [41] is in agreement with the mechanism reported in Eqs. (11a)–(11d). The stages obtained during the decomposition of $Pr(NO_3)_3{\cdot}6H_2O$ represented by Eqs. (12a)–(12b) are also in agreement with the findings of Hussein [34] who reported the formation of praseodymium oxide from the thermal decomposition of hydrated praseodymium acetate and oxalate.

Conclusions

The kinetics and mechanism of thermal decomposition of five lighter rare earth metal precursors, namely $Ce(NO_3)_3{\cdot}6H_2O$, $La(NO_3)_3{\cdot}6H_2O$, $Sm(NO_3)_3{\cdot}6H_2O$, $Nd(NO_3)_3{\cdot}6H_2O$ and $Pr(NO_3)_3{\cdot}6H_2O$, have been investigated by thermogravimetric analysis. The thermal decomposition of the rare earth metal precursors produced corresponding rare earth metal oxides (CeO_2, La_2O_3, Sm_2O_3, Nd_2O_3 and Pr_2O_3, respectively) with activation energies of 230.26, 344.78, 320.20, 392.72 and 258.26 kJ mol^{-1} from Kissinger model and 229.01, 350.56, 348.56, 392.72 and 388.56 kJ mol^{-1} using Ozawa–Flynn–Wall model. The FTIR analysis of both the precursors and the metal oxides shows a distinct difference in their respective chemical composition which is confirmed by the disappearance of the OH– and NO– bonds in the rare earth metal oxides. Further analysis of the kinetic data using Coat–Redfern models showed that two-dimensional mechanism with activation energies of 105.61, 107.61, 140.61, 144.52 and 154.78 kJ mol^{-1} for thermal decomposition of $Ce(NO_3)_3{\cdot}6H_2O$, $La(NO_3)_3{\cdot}6H_2O$, $Sm(NO_3)_3{\cdot}6H_2O$, $Nd(NO_3)_3{\cdot}6H_2O$ and $Pr(NO_3)_3{\cdot}6H_2O$, respectively, best described the solid-state decomposition reaction. The findings from the present study show that the rare earth metal nitrate hexahydrates are good precursors for synthesis of rare earth metal oxides such CeO_2, La_2O_3, Sm_2O_3, Nd_2O_3 and Pr_2O_3 which can be used as supports, promoters and catalyst in reaction such as catalytic methane reforming.

Acknowledgements The authors would like to acknowledge the research fund RDU130501 granted by the Ministry of Science, Technology and Innovation Malaysia (MOSTI) and the DSS scholarship granted to Bamidele V. Ayodele by the Universiti Malaysia Pahang.

References

1. Hedrick JB. Rare-earth metals. US Geol Surv 1998:61.1–61.12. http://minerals.usgs.gov/minerals/pubs/commodity/rare_earths/740497.pdf.
2. Alonso E, Sherman AM, Wallington TJ, Everson MP, Field FR, Roth R, et al. Evaluating rare earth element availability: a case with revolutionary demand from clean technologies. Environ Sci Technol. 2010;46:3406–14. doi:10.1021/es203518d.
3. Sato S, Takahashi R, Kobune M, Gotoh H. Basic properties of rare earth oxides. Appl Catal A Gen. 2009;356:57–63. doi:10.1016/j.apcata.2008.12.019.
4. Igarashi A, Ichikawa N, Sato S, Takahashi R, Sodesawa T. Dehydration of butanediols over CeO_2 catalysts with different particle sizes. Appl Catal A Gen. 2006;300:50–7. doi:10.1016/j.apcata.2005.10.054.
5. Sato S, Takahashi R, Kobune M, Inoue H, Izawa Y, Ohno H, et al. Dehydration of 1,4-butanediol over rare earth oxides. Appl Catal A Gen. 2009;356:64–71. doi:10.1016/j.apcata.2008.12.017.
6. Igarashi A, Sato S, Takahashi R, Sodesawa T, Kobune M. Dehydration of 1,4-butanediol over lanthanide oxides. Catal Commun. 2007;8:807–10. doi:10.1016/j.catcom.2006.09.003.
7. Sato S. Dehydration of 1,4-butanediol into 3-buten-1-ol catalyzed by ceria. Catal Commun. 2004;5:397–400. doi:10.1016/j.catcom.2004.05.006.
8. Ayodele BV, Khan MR, Cheng CK. Syngas production from CO_2 reforming of methane over ceria supported cobalt catalyst: effects of reactants partial pressure. J Nat Gas Sci Eng. 2015;. doi:10.1016/j.jngse.2015.09.049.
9. Therdthianwong S, Therdthianwong A, Siangchin C, Yongprapat S. Synthesis gas production from dry reforming of methane over Ni/Al_2O_3 stabilized by ZrO_2. Int J Hydrogen Energy. 2008;33:991–9. doi:10.1016/j.ijhydene.2007.11.029.
10. Laosiripojana N, Sutthisripok W, Assabumrungrat S. Synthesis gas production from dry reforming of methane over CeO_2 doped Ni/Al_2O_3: influence of the doping ceria on the resistance toward carbon formation. Chem Eng J. 2005;112:13–22. doi:10.1016/j.cej.2005.06.003.
11. Zhang B, Cai W, Li Y, Xu Y, Shen W. Hydrogen production by steam reforming of ethanol over an Ir/CeO_2 catalyst: reaction mechanism and stability of the catalyst. Int J Hydrogen Energy. 2008;33:4377–86. doi:10.1016/j.ijhydene.2008.05.022.
12. Xu W, Si R, Senanayake SD, Llorca J, Idriss H, Stacchiola D, et al. In situ studies of CeO_2-supported Pt, Ru, and Pt–Ru alloy catalysts for the water–gas shift reaction: active phases and reaction intermediates. J Catal. 2012;291:117–26. doi:10.1016/j.jcat.2012.04.013.

13. Wang H, Liu Y, Wang L, Qin YN. Study on the carbon deposition in steam reforming of ethanol over Co/CeO_2 catalyst. Chem Eng J. 2008;145:25–31. doi:10.1016/j.cej.2008.02.021.
14. Verykios XE. Catalytic dry reforming of natural gas for the production of chemicals and hydrogen. Int J Hydrogen Energy. 2003;28:1045–63. doi:10.1016/S0360-3199(02)00215-X.
15. Abasaeed AE, Al-fatesh AS, Naeem MA, Ibrahim AA, Fakeeha AH. Catalytic performance of CeO_2 and ZrO_2 supported Co catalysts for hydrogen production via dry reforming of methane. Int Hydrogen Energy. 2015:6818–26. doi:10.1016/j.ijhydene.2015.03.152.
16. Ayodele BV, Cheng CK. Modelling and optimization of syngas production from methane dry reforming over ceria-supported cobalt catalyst using artificial neural networks and Box–Behnken design. J Ind Eng Chem. 2015;. doi:10.1016/j.jiec.2015.08.021.
17. Ayodele BV, Khan MR, Lam SS, Cheng CK. Production of CO-rich hydrogen from methane dry reforming over lanthania-supported cobalt catalyst: kinetic and mechanistic studies. Int J Hydrogen Energy. 2016;. doi:10.1016/j.ijhydene.2016.01.091.
18. Ayodele BV, Khan MR, Cheng CK. Catalytic performance of ceria-supported cobalt catalyst for CO-rich hydrogen production from dry reforming of methane. Int J Hydrogen Energy. 2015;. doi:10.1016/j.ijhydene.2015.10.049.
19. Wendlandt W. Thermal decomposition of scandium, yttrium, and rare earth metal oxalates. Anal Chem. 1958;30:58–61.
20. Wendlandt WW. The thermal decomposition of the heavier rare earth metal chloride hydrates. J Inorg Nucl Chem. 1959;9:136–9. doi:10.1016/0022-1902(59)80072-5.
21. Wendlandt WW. The thermal decomposition of yttrium, scandium, and some rare-earth chloride hydrates. J Inorg Nucl Chem. 1957;5:118–22. doi:10.1016/0022-1902(57)80052-9.
22. Wendlandt WW. The thermolysis of the rare earth and other metal nitrates. Anal Chim Acta. 1956;15:435–9. doi:10.1016/0003-2670(56)80082-2.
23. Im G. Low-temperature molar heat capacity and thermodynamic properties of rare earth complex. J Therm Anal Calorim. 2016;124:429–35. doi:10.1007/s10973-015-5133-8.
24. Zapa BL, Zapa W. Synthesis, spectral and thermal study of La (III), Nd(III), Sm(III), Eu(III), Gd(III) and Tb(III) complexes with mefenamic acid. J Therm Anal Calorim. 2016:363–74. doi:10.1007/s10973-015-5120-0.
25. Novikov VV, Mitroshenkov NV, Matovnikov AV, Avdashchenko DV, Trubnickov SV, Morozov AV. Peculiarities of the lattice thermal properties of rare-earth tetraborides. J Therm Anal Calorim. 2015:1597–602. doi:10.1007/s10973-015-4475-6.
26. Hussein GAM. Rare earth metal oxides: formation, characterization and catalytic activity thermoanalytical and applied pyrolysis review. J Anal Appl Pyrolysis. 1996;37:111–49. doi:10.1016/0165-2370(96)00941-2.
27. Blaine RL, Kissinger HE. Homer Kissinger and the Kissinger equation. Thermochim Acta. 2012;540:1–6. doi:10.1016/j.tca.2012.04.008.
28. Aboulkas A, El harfi K, El Bouadili A. Thermal degradation behaviors of polyethylene and polypropylene. Part I: pyrolysis kinetics and mechanisms. Energy Convers Manag. 2010;51:1363–9. doi:10.1016/j.enconman.2009.12.017.
29. Ebrahimi-Kahrizsangi R, Abbasi MH. Evaluation of reliability of Coats–Redfern method for kinetic analysis of non-isothermal TGA. Trans Nonferrous Metals Soc China. 2007;18:2–6.
30. Ozawa T. A new method of analyzing thermogravimetric data. Bull Chem Soc Jpn. 1965;38:1881–6. doi:10.1246/bcsj.38.1881.
31. Yao F, Wu Q, Lei Y, Guo W, Xu Y. Thermal decomposition kinetics of natural fibers: activation energy with dynamic thermogravimetric analysis. Polym Degrad Stab. 2008;93:90–8. doi:10.1016/j.polymdegradstab.2007.10.012.
32. Melnikov P, Arkhangelsky IV, Nascimento VA, Silva AF, Consolo LZZ. Thermolysis mechanism of samarium nitrate hexahydrate. J Therm Anal Calorim. 2014:1537–41. doi:10.1007/s10973-014-4067-x.
33. Strydom C, van Vuuren CP. The thermal decomposition of Cerium(I11) nitrate hydrate. J Therm Anal. 1987;32:157–60.
34. Hussein GAM. Formation of praseodymium oxide from the thermal decomposition of hydrated praseodymium acetate and oxalate. J Anal Appl Pyrolysis. 1994;29:89–102. doi:10.1016/0165-2370(93)00782-I.
35. Balboul BAA, Myhoub AYZ. The characterization of the formation course of neodymium oxide from different precursors: a study of thermal decomposition and combustion processes. J Anal Appl Pyrolysis. 2010;89:95–101. doi:10.1016/j.jaap.2010.06.003.
36. Ihli J, Wong WC, Noel EH, Kim Y-Y, Kulak AN, Christenson HK, et al. Dehydration and crystallization of amorphous calcium carbonate in solution and in air. Nat Commun. 2014;5:3169. doi:10.1038/ncomms4169.
37. Arii T, KIshi A, Ogawa M, Sawada Y. Thermal decomposition of cerium (III) acetate hydrate by a three-dimensional thermal analysis. Anal Sci. 2001;17:875.
38. Premkumar T, Govindarajan S, Coles AE, Wight CA. Thermal decomposition kinetics of hydrazinium cerium 2,3-pyrazinedicarboxylate hydrate: a new precursor for CeO_2. J Phys Chem B. 2005;109:6126–9. doi:10.1021/jp0445223.
39. Todorovsky DS, Getsova MM, Vasileva MA. Thermal decomposition of lanthanum-titanium citric complexes prepared from ethylene glycol medium. J Mater Sci. 2002;37:4029–39. doi:10.1023/A:1019600815906.
40. Hussein GAM, Buttrey DJ, DeSanto P, Abd-Elgaber AA, Roshdy H, Myhoub AYZ. Formation and characterization of samarium oxide generated from different precursors. Thermochim Acta. 2003;402:27–36. doi:10.1016/S0040-6031(02)00535-X.
41. Kępiński L, Zawadzki M, Miśta W. Hydrothermal synthesis of precursors of neodymium oxide nanoparticles. Solid State Sci. 2004;6:1327–36. doi:10.1016/j.solidstatesciences.2004.07.003.